Development of Understanding of The Interaction between Localized deformation and SCC of Austenitic Stainless Steels Exposed to Primary Environment

Thierry Couvant, Laurent Legras, Antoine Herbelin, Andrey Musienko,
Gabriel Ilbevare, David Delafosse, Georges Cailletaud, J. Hickling

DEVELOPMENT OF UNDERSTANDING OF THE INTERACTION BETWEEN LOCALIZED DEFORMATION AND SCC OF AUSTENITIC STAINLESS STEELS EXPOSED TO PRIMARY PWR ENVIRONMENT

T. Couvant [1], L. Legras [1], A. Herbelin [1], A. Musienko [2], G. Ilevbare [3], D. Delafosse [4], G. Cailletaud [2], J. Hickling [5]

[1] EDF R&D - MMC, Route de Sens, 77818 Moret-sur-Loing, France
[2] ENSMP, Evry, France
[3] ENSM-SE, 157 Cours Fauriel, 42023 St-Etienne cedex 2, France
[4] EPRI, Palo Alto, USA
[5] CMC, Cyprus

Understanding and quantification of interactions between localized deformation in materials and environmental-assisted cracking (EAC) could play an important role in maintaining the integrity of LWR components. Thus, a detailed understanding of strain localization during plastic deformation and of the underlying mechanisms is of great importance for the manufacturing and design of materials exposed to the environment of the primary circuit of PWRs. Thus, the crystal plasticity law of a 304L austenitic stainless steel has been identified, in order to quantify the effect of a change of strain path on the strain localization and increase the understanding of the contribution of the strain hardening and the strain incompatibilities on the mechanisms of initiation of SCC. Pre-deformation of the specimens used for SCC tests was evaluated using image correlation. Constant elongation rate tests and constant elongation tests were conducted for different levels of pre-deformations ($0.07 < \varepsilon < 0.18$). Examinations indicated the severe and deleterious effect of the strain localization due to a change of strain path on intergranular SCC susceptibility. Intergranular cracks initiated systematically in the low-deformed areas, where limited deformation (less than 1%) occurred during the exposure to the environment, and where high stress levels due to strain incompatibilities are expected.

1. INTRODUCTION

Understanding and quantification of interactions between localized deformation in materials and environmental-assisted cracking (EAC) could play an important role in maintaining the integrity of LWR components. A previous (1) review of the different types of identified strain localization-EAC interactions allowed key gaps to be identified. Thus, a detailed understanding of strain localization during plastic deformation and of the underlying mechanisms is important for the manufacture and design of materials exposed to the environment of the primary circuit of PWRs. Previous studies (2) have demonstrated the deleterious effect of cross tests on susceptibility of 304L to IGSCC in PWR primary water at 360°C. This result has been interpreted by the authors as a consequence of strain localization induced by orthogonal strain paths as defined by Schmitt (3). The objectives of this study were to correlate strain localization and selective oxidation using approaches based on quantitative and fundamental understanding, in order to evaluate the relevance of interactions between localized deformation and stress corrosion cracking (SCC) in austenitic alloys exposed to a PWR primary water. Thus, a wide range of techniques was deployed in this program to characterize the microstructures, to quantify strain localization and associated oxidation.

2. MATERIALS

Austenitic alloys tested in this work (304L and 316L) are 30-mm-thick plates. Chemical compositions and mechanical properties of the materials as manufactured are given in Table 1 and Table 2, respectively. Unlike 316L, 304L contains less than 5% of residual δ-ferrite and is subject to strain-induced martensite transformation: $Ms = -133°C$, $Md_{30} = -3°C$, as predicted by Angel (4). Concerning the 316L heat, $Ms = -133°C$, $Md_{30} = -40°C$. The staking fault energy (SFE) of 304L is 24 mJ.m^{-2} and 33 mJ.m^{-2} for 316L (5). Non-sensitized 304L and 316L were solution annealed at 1050°C and water quenched. The resultant microstructures, with no evidence of any carbide precipitates in the matrix or along the grain boundaries, were characterized using EBSD. Mean grain diameter is 27 µm for 304L and 90 µm for 316L. The distribution of misorientation angles in the range $6° < \phi < 59°$, including twin boundaries ($\phi > 54°$). Distributions are very similar for 304L and 316L. Thus, in these two materials, 30 to 50% of boundaries are twin boundaries. Misorientation angles in the range $37° < \phi < 54°$ correspond to about 30% of the boundaries. Inverse pole figures are given in Figure 1, at the same scale.

Table 1 – Chemical composition (wt. %).

Material	Heat	C (%)	S (%)	P (%)	Si (%)	Mn (%)	Fe (%)	Ni (%)	Cr (%)	Mo (%)	N (%)	Al (%)
316L	XY183	0.026	0.004	0.033	0.42	1.81	65.75	12.00	17.34	2.57	0.050	-
AISI Requirement for 316L		< 0.03	< 0.03	< 0.045	< 1	< 2		10-13	16.5-18.5	2-2.5	< 0.11	
304L	T2575	0.026	0.002	0.027	0.52	1.49	68.68	9.45	19.23	0.24	0.064	0.033
AISI Requirement for 304L		< 0.03	< 0.03	< 0.045	< 1	< 2		8-10	18-20		< 0.11	

Table 2 – Mechanical properties in air at room temperature.

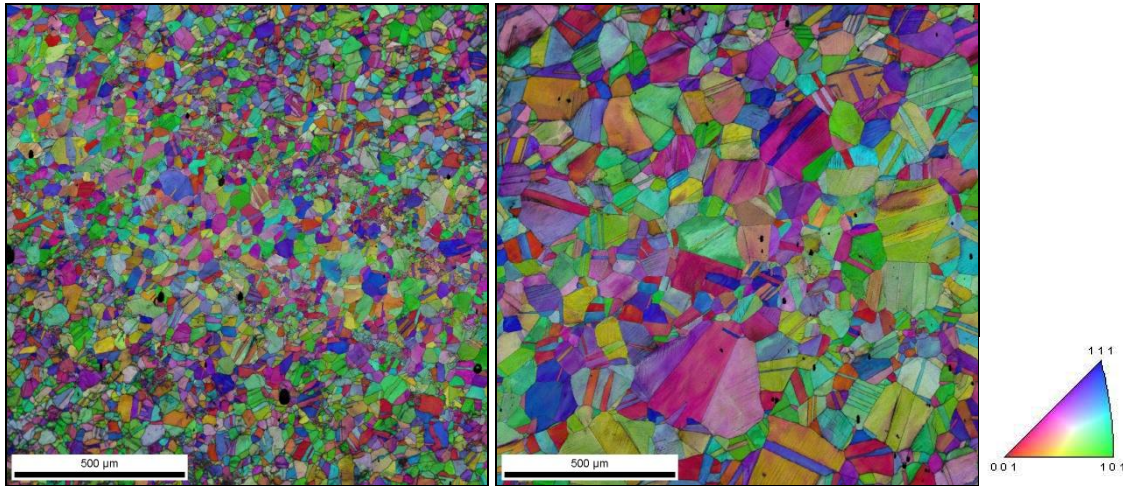| Material	Heat	$Ys_{0,2}$ (MPa)	UTS (MPa)	El. (%)	HV_{30}
316L	XY183	255	553	63	
304L	T2575	247	582	60	160
RCCM-M220 requirement		> 170	> 500	> 45	126-179

Figure 1 – Example of inverse pole figures of 304L (left) and 316L (right) at similar scales.

3. APPROACH

3.1. Specimens

Cross tests were used to promote strain localization (Figure 2). This design was optimized to guaranty strain localization in the cross-area of the specimen during prior-straining and second deformation in primary water and to avoid significant deleterious deformation in specimen fillets. The specimen is not symmetrical: only the front face is perfectly plane, designed to perform an easy mechanical polishing, material characterization and local strain evaluation. All characterizations and observations were done on 1 mm² at the center of the specimen's front face, prepared as described below:

- Three-step local polishing of each specimen, including mechanical polishing (0.04 µm finish) to remove superficial cold work, electropolishing (20°C, 19 V) in Struers A2 electrolyte A2 solution containing 73% ethanol, 10% butoxyethanol, 9% water, and 8% perchloric acid, and ionic polishing to remove the chemically affected superficial metal layer for relevant oxidation characterization.

- EBSD characterization at the center of each specimen (1 mm²).

- Grid deposition (1 mm², mesh size = 5 µm), by electronic micro lithography, at the center

of the specimens using the following procedure: the center of the sample is coated by centrifugation with about 200 nm of a photosensitive polymer (poly methyl metacrylate). After heating (30 min at 135°C), the sample is locally irradiated (4 C/m²) by a SEM beam (tension of acceleration = 30 kV, probe current = 3 nA, working distance = 30 mm), drawing a grid. The irradiated resin is then dissolved in a solution composed of methyl cetone (35%) and isopropylic alcohol (65%). A thin layer of gold is then deposited, first by cathodic pulverization, then by evaporation under vacuum. Residual resin is eliminated in a solution of ethyl acetate.

All cross specimens were finally prior deformed in ambient air, along $\vec{X}$ axis.

3.2. Tensile tests

After pre-straining, a final machining of specimens is achieved by cutting off the arms used for pres-straining to insure that deformation will be localized at the center of the specimen during the second loading at 360°C (Figure 2). Specimens were ultrasonically rinsed in ethanol and then in distilled water. Tests were carried out in Hastelloy (C-276) autoclaves. Specimens were insulated from the autoclave by oxidized Zircalloy to avoid galvanic coupling. Experiments were conducted

under open circuit conditions. The environment was primary water (1000 ppm B as boric acid, 2 ppm Li as lithium hydroxide) at 360°C. The solution was previously de-aerated by evaporating 20% of the initial volume at 125°C, then hydrogen overpressure was introduced (30 cm^3.kg^{-1}) and controlled using a Pd-Ag probe. The chemistry was analyzed and validated before each test (B, Li, Cl$^-$, SO$_4^{2-}$, F$^-$). Pre-oxidation (5-7 days) in a primary water test environment was performed.
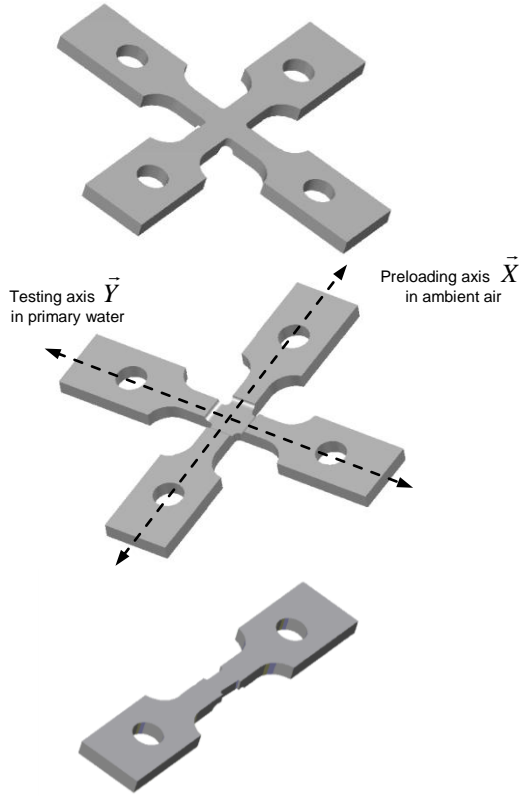

Figure 2 – Front (left) and back (center) faces of the cross specimen for prior deformation in ambient air. Specimen after final machining for testing at 360°C along $\vec{Y}$ axis.

3.3. Image displacement analysis

Gridline images are collected before and after each step of deformation using scanning electron microscopy (SEM). All data are collected for the same working distance. Comparison of the grid before and after deformation reveals the material superficial displacement field used for evaluating deformation gradient tensor $\tilde{F}$:

$$\vec{x}_0 = \tilde{F}.\vec{x}_1 \qquad (1)$$

where $\vec{x}_0$ is a vector in the initial configuration (before deformation), while $\vec{x}_1$ is the corresponding vector in the intermediate configuration (after prior-deformation in air) or in the final configuration (after the deformation in the primary water). At each node of the grid, $\tilde{F}$ is evaluated using the four nearest nodes. Finally, Green Lagrange

tensor $\tilde{E}$ is calculated at each node of the mesh using (2:

$$\tilde{E} = \frac{1}{2}\left(\tilde{F}^T \tilde{F} - \tilde{I}\right) \qquad (2)$$

where $\tilde{F}^T$ is the transposed tensor of $\tilde{F}$.

3.4. Electronic microscopy

All specimens were examined by SEM after completion of testing in primary water, in order to identify sites of initiation. A dual-beam Helios Nanolab from FEI (SEM equipped with a Focused Ions Beam column) was used for preparing cross section thin foils on specifically deformed locations. This dual beam has a Schottky field emission gun column, Ga ion beam column, Pt and C gas injection system, carbon selective etching system, EDX detector and Autoprobe internal micromanipulator. TEM observations of specimens were performed using a FEI TECNAI G2 FEG STEM equipped with Gatan Imaging Filter, EDAX energy dispersive spectrometer and HAADF detector.

3.5. Finite element modeling

Crystal plasticity modeling is an appropriate approach to evaluate the heterogeneity of the continuous mechanical response in an aggregate, taking into account activation of slip systems. Therefore, such modeling is a relevant tool for comprehending SCC mechanisms, where strain hardening and strain incompatibilities play a significant role in the cracking mechanism. In the present modeling, the strain rate $\tilde{\dot{\varepsilon}}$ was first decomposed into elastic $\tilde{\dot{\varepsilon}}^e$ and plastic $\tilde{\dot{\varepsilon}}^p$ parts (Equation 3).

$$\tilde{\dot{\varepsilon}} = \tilde{\dot{\varepsilon}}^e + \tilde{\dot{\varepsilon}}^p \qquad (3)$$

Considering that intragranular deformation is the main contribution, plastic strain rate $\tilde{\dot{\varepsilon}}_p$ in a grain is the sum of elementary shear rates $\dot{\gamma}^s$ extending over all active slip systems s (Equation 4):

$$\tilde{\dot{\varepsilon}}^p = \sum_s \frac{\dot{\gamma}^s}{2}\left(\overline{m}^s \otimes \overline{n}^s + \overline{n}^s \otimes \overline{m}^s\right) \qquad (4)$$

where $\overline{n}^s$ is normal vector to the slip plane and $\overline{m}^s$ is a vector corresponding to slip direction. Twelve $\{1\,1\,1\}\ \langle 110\rangle$ octahedral systems were assumed to be potentially active. Crystal plasticity models rely on the understanding that plastic deformation in crystals at low temperatures occurs by crystallographic slip following Schmidt's law. Thus, following the Schmidt law, each elementary slip rate $\dot{\gamma}^s$ depends on resolved shear stress τ^s. The shear rate $\dot{\gamma}^s$ links to the motion of

dislocations in active slip systems. Thus, flow rule $\dot{\gamma}^s$ is described by a phenomenological Norton-like viscoplastic relation (Equation 5), where K_s is viscosity constant, n_s is stress sensitivity, and τ_c^s is the critical resolved shear stress on s:

$$\dot{\gamma}^s = \left\langle \frac{\left|\tau^s - x^s\right| - \tau_c^s}{K_s} \right\rangle^{n_s} \frac{(\tau^s - x^s)}{\left|\tau^s - x^s\right|} \qquad (5)$$

Resolved shear stress τ^s on slip system s is the projection of the stress tensor on orientation tensor $\tilde{m}^s$ (Equation 6):

$$\tau^s = \tilde{\sigma} : \tilde{m}^s \qquad (6)$$

x^s is the kinematic hardening, proportional to α^s (Equations 7 and 8):

$$x^s = c\,\alpha^s \qquad (7)$$

$$\dot{\alpha}^s = \dot{\gamma}^s - d\alpha^s\left|\dot{\gamma}^s\right| \qquad (8)$$

where c is a constant. τ_c^s is the isotropic hardening, depending on cumulated strain γ_{cum}^r (Equations 9 and 10):

$$\tau_c^s = \tau_0 + Q\sum_r h_{rs}\left(1 - \exp(-b\gamma_{cum}^r)\right) \qquad (9)$$

$$\gamma_{cum}^r = \int_t \left|\dot{\gamma}^r\right| dt \qquad (10)$$

where h is an interaction matrix, describing the self hardening (diagonal components) due to the interactions between coplanar slip systems, and the latent hardening (non-diagonal components) due to the interactions between secant slip systems. All components h_{rs} of h are normalized by the self-hardening components. When strain hardening is isotropic, it is independent of the active slip system. Therefore, in this situation $h_{sr} = 1$. Usually, self-hardening components are inferior to latent components. Both isotropic and kinematic hardenings are considered when modeling the behavior of the material. Nevertheless, in a first approach (6), it is assumed that $h_{rs} = 1$.

One free mesh has been produced, using Voronoi space subdivision, with 343 grains, 2174653 nodes, and 1599480 tetrahedral elements with 10 nodes (type c3d10), as shown in Figure 3. The finite element calculations were performed with the code Zebulon (7).
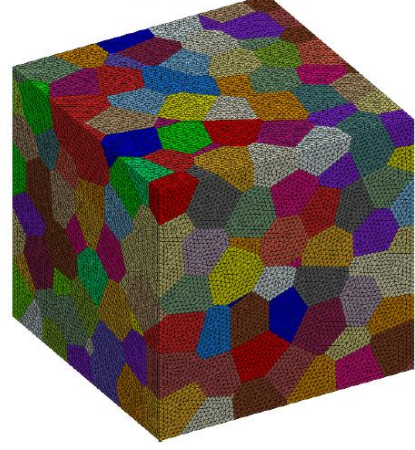

Figure 3 – 3D finite element mesh with 343 grains, 2174653 nodes, and 1599480 elements c3d10.

5. RESULTS OF EXPERIMENTS

5.1. Strain localization after prior deformation

Results are given in Table 3. Prior mean equivalent strains E_{eq} are within the range 0.065-0186.

Figure 4 is an E_{eq} mapping at the surface of specimen 1594-T112-06, considering an area of 250 µm × 250 µm. Strain is localized in slip bands oriented at ± 45° from the main axis load $\vec{x}$. Strain level in intense slip bands is typically two times higher than the mean deformation value. Between the intense slip bands, areas with only few percent of strain are observed. Figure 5 is an example of frequency of prior E_{eq} observed at the surface of specimen 1594-T217-02. The E_{eq} distribution is Gaussian.

Standard deviations of prior E_{eq}, $SD(E_{eq})$, measured on specimens are reported in Table 3, and plotted in Figure 6 against E_{eq}. This figure shows the increase of $SD(E_{eq})$ with E_{eq}. (11 is a fit of data plotted in Figure 6 that could be used to predict the Gaussian distribution of equivalent strain associated to a known mean value.

$$SD(E_{eq}) = 0.35\,E_{eq} \qquad (11)$$

Typically, the range of E_{eq}, E_{xx}, and E_{yy} is two times higher than their mean value.

Figure 7 gives the evolution of the deformation as a function of the analyzed area, and shows that an analyze limited to 100 µm × 100 µm is sufficient for a good estimation of the mean, maximum, and minimum values of the different components of E. This means that an aggregate of tens of grains is sufficient to estimate with good precision the mean deformation of stainless steels and its heterogeneity.

Table 3 – Mean prior-deformation (in $\vec{x}$ direction) in ambient air.

| Material	Specimen	Analyzed area (mm²)	Mean(E_{xx})	Mean(E_{yy})	Mean(E_{xy})	Mean($\dot{E}_{xx}$) (s^{-1})	Mean(E_{eq})	SD(E_{eq})	RES(E_{eq}) (mm²)
304L	1594-T112-02	0.01	0.120	-	-	10^{-3}	-	-	-
	1594-T112-07	0.12	0.110	− 0.018	0.006	1.2 10^{-3}	0.136	0.050	-
	1594-T112-03	0.50	0.115	− 0.024	− 0.003	1.6 10^{-3}	0.127	0.037	0.014
	1594-T112-04	0.04	0.069	− 0.047	0.001	1.0 10^{-3}	0.070	0.025	-
	1594-T112-06	0.06	0.087	− 0.055	0.000	1.0 10^{-3}	0.088	0.038	0.016
	1594-T112-08	0.01	0.178	− 0.089	0.016	1.0 10^{-3}	0.186	0.068	-
316L	1594-T217-01	0.50	0.066	− 0.047	0.001	1.3 10^{-3}	0.073	0.038	0.103
	1594-T217-02	0.01	0.038	− 0.029	0.000	1.1 10^{-3}	0.043	-	-
	1594-T217-04	0.29	0.077	− 0.047	− 0.005	1.5 10^{-3}	0.085	0.037	0.045
	1594-T217-07	0.01	0.065	−0.056	− 0.002	1.1 10^{-3}	0.075	0.028	-
	1594-T217-08	0.01	0.156	− 0.069	0.013	1.5 10^{-3}	0.159	0.044	-
	1594-T217-10	0.04	0.065	− 0.039	0.005	1.0 10^{-3}	0.069	0.026	-
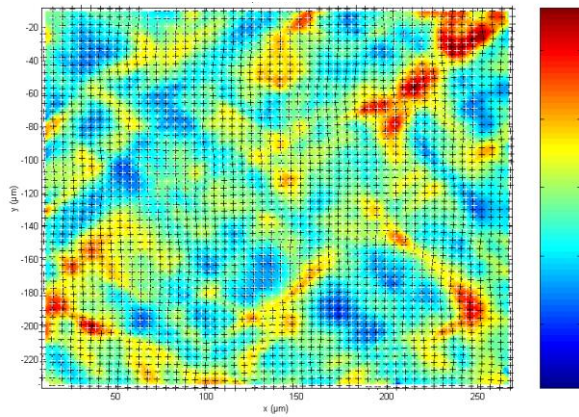
Figure 4 – Map of equivalent deformation evaluated at the surface of specimen 1594-T112-06 (304L). Analyzed area = 0.06 mm².
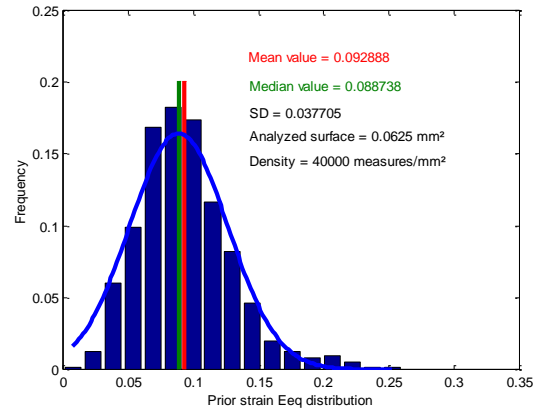

Figure 5 – Evolution of min., mean, median, max. deformation E_{eq} and SD versus analyzed surface (40000 measures.mm^{-2}) of specimen 1594-T217-01 (316L).
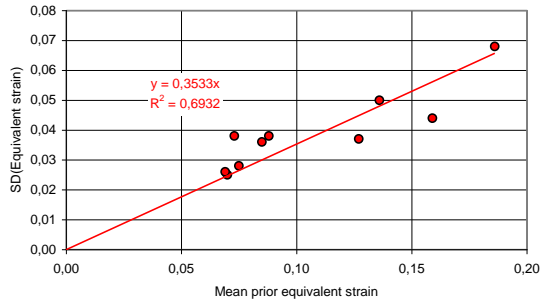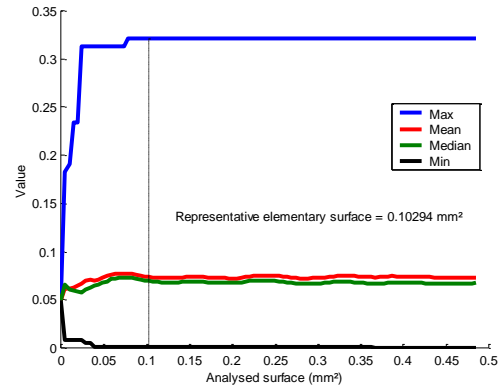

Figure 6 – Evolution of SD(E_{eq}) versus mean(E_{eq}) for 10 prior-deformed specimens.

Figure 7 – Evolution of min., mean, median, max. deformation E_{eq} and SD versus analyzed surface (40000 measures.mm^{-2}) of specimen 1594-T217-01 (316L).

5.2. Initiation of SCC in primary water

Results of constant elongation rate tests in primary water are presented in Table 4. Strain and strain rates are within the ranges 0.003 − 0.500 and 1.4 10^{-9} s^{-1} − 9.9 10^{-8} s^{-1} respectively. As expected, initiation of SCC was essentially intergranular.

The test on specimen 1594-T112-02 was interrupted for SEM examination after 270 hours of tension in a primary hydrogenated environment at 360°C. No initiation of SCC was noticed. Then, the specimen was tested again up to failure. Observations of the fracture surface indicated a preferential intergranular initiation in the pre-strained area of the specimen (Figure 8). By contrast SCC propagation was essentially transgranular in the most deformed part of the specimen (Figure 9). This result indicates that IGSCC was enhanced by the change of strain path after prior deformation, while TGSCC was clearly promoted by the continuous deformation during testing.

Test on specimen 1594-T112-07 indicated an important susceptibility to IGSCC for a limited exposure to primary water (313 h). Prior

deformation E_{xx} and second deformation E_{yy} levels were similar. By contrast, prior (prior E_{xx} = 0.17) and second (second E_{yy} < 0.01) deformations applied to specimen 1594-T112-08 were completely different. However, significant IGSCC initiation was observed on both specimens. Therefore, intergranular cracking resulted in the change of strain path, and large deformation during exposure to the environment is not required for IG cracking.
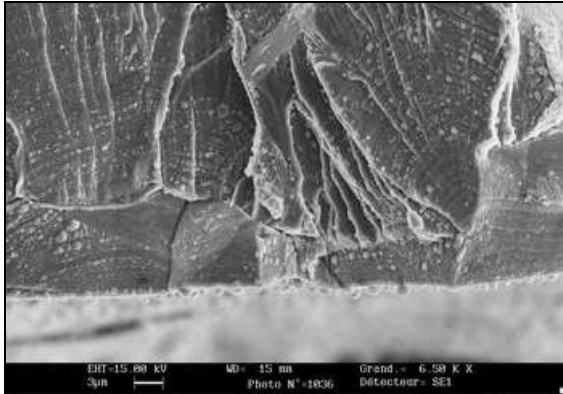

Figure 8 – IGSCC initiation followed by transition to TGSCC on fracture surface of specimen 1594-T112-2 after 1400 h of tension in primary environment.
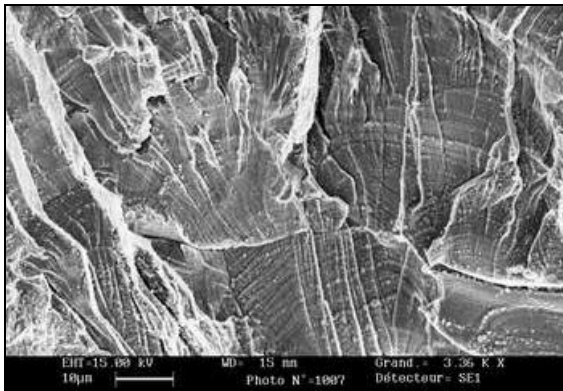

Figure 9 – TGSCC propagation on fracture surface of specimen 1594-T112-2 after 1400 h of tension in primary environment.

Test on specimen 1594-T217-01 (316L) revealed a shallow intergranular initiation (Figure 10) appropriate for local strain evaluations. By constrast intergranular cracks were too opened in the case of specimen 1594-T217-02 (Figure 11). TGSCC was also noticed on this specimen.

No initiation was observed on specimen 1594-T217-10 after 577 h in primary water, for a prior deformation similar to those of specimen 1594-T217-01 and a limited second deformation (E_{yy} = 0.003). Thus, time to initiation probably decreases when prior and second strain levels increase.

One test was conducted under constant displacement on specimen 1594-T112-03. Based on previous results [9], no relaxation was expected during the SCC test (1864 hours). A limited number of intergranular cracks were observed. Slip line traces are observed on the flanks of the cracks. This result suggests that IGSCC initiation is possible under constant load following a complex strain path when the second strain is limited.

Correlation between initiation and local deformation E_{yy} in primary water is illustrated in Figure 12 and Figure 13. These figures indicate that SCC initiated at grain boundary where local strain gradients are significant. Therefore, an important effect of strain incompatibilities on intergranular cracking is expected. The cracked grain boundaries were in addition favorably oriented for cracking against loading axis.

Non-initiation (gray dots), IG- (red crosses) and TGSCC initiation (blue crosses) conditions are plotted against prior deformation E_{xx} in ambient air, second deformation E_{yy} in primary water in Figure 14. 0.3 mm² of the surface of the specimen 1594-T217-01 were analyzed, including 12182 measures of strain. 418 nodes were considered as representative sites for initiation. Most of the cracks were intergranular, confirming the appropriate design and loading used in this study to investigate IGSCC. No crack initiated where deformation was compressive during the exposure to primary water (Second E_{yy} < 0). Most of the cracks initiated for 0.05 < prior-E_{xx} < 0.1 and 0.01 < second-E_{yy} < 0.04. It is confirmed that high levels of deformation during the exposure to the primary water are not necessary to initiate.

Table 4 – Results of tensile tests (in $\vec{y}$ direction) in a primary PWR environment at 360°C.

| Material	Specimen	Mean Prior-E_{xx}	Duration (h)	Mean E_{yy}	Mean $\dot{E}_{yy}$ (s^{-1})	Remarks
304L	1594-T112-02	0.120	1400	≈ 0.500	≈ 9.9 10^{-8}	No initiation after 270 h. Initiation of IGSCC then TGSCC propagation up to failure.
	1594-T112-06	0.070	519	0.040	2.1 10^{-8}	Significant IGSCC initiation + shallow TGSCC initiation
	1594-T112-07	0.100	313	0.110	9.8 10^{-8}	Significant IGSCC initiation + shallow TGSCC initiation
	1594-T112-08	0.170	430	0.006	3.9 10^{-9}	Significant IGSCC initiation + shallow TGSCC initiation
	1594-T112-03	0.111	1864	0.010	0	Few sites of IGSCC
316L	1594-T217-01	0.066	720	0.020	7.7 10^{-9}	Shallow IGSCC initiation
	1594-T217-02	0.040	1606	0.270	4.7 10^{-8}	Significant IGSCC initiation + TGSCC
	1594-T217-10	0.060	577	0.003	1.4 10^{-9}	No initiation
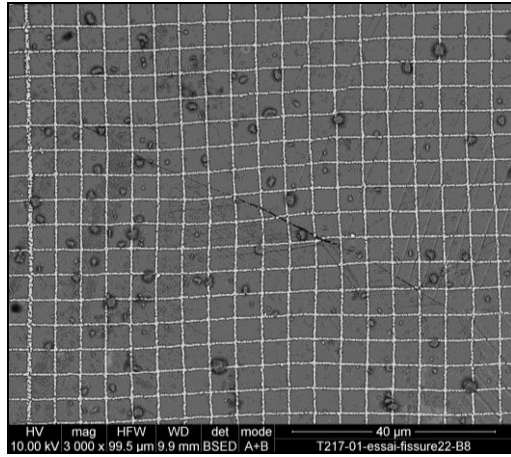
Figure 10 – IGSCC initiation on specimen 1594-T217-1 after 720 h of tension in primary environment.
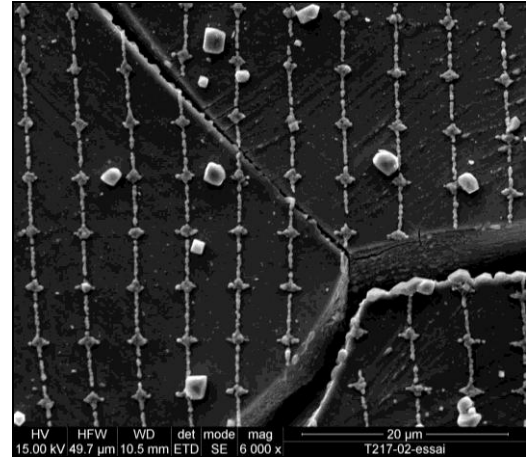

Figure 11 – IGSCC initiation on specimen 1594-T217-2 after 1600 h of tension in primary environment.
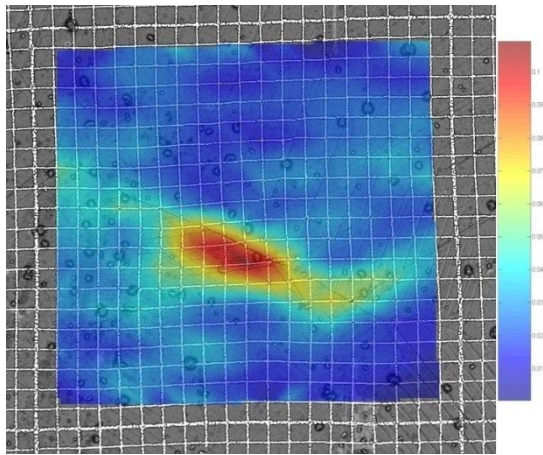

Figure 12 – Deformation E_{yy} (in primary water) at the surface of specimen 1594-T217-1 (316L) after testing in a primary water (360°C).
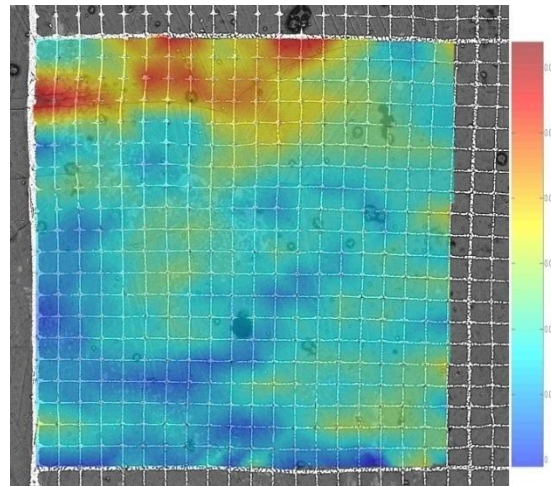

Figure 13 – Deformation E_{yy} (in primary water) at the surface of specimen 1594-T217-1 (316L) after testing in a primary water (360°C).
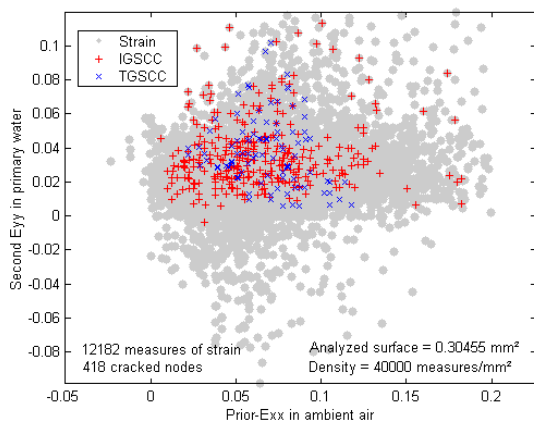

Figure 14 – Preferential conditions for SCC initiation as a function of prior deformation in ambient air and second strain in primary water. Specimen 1594-T217-01 (316L) after testing in a primary water (360°C).

5.3. Oxide characterization

Several sites of sampling were chosen at the surface of specimens 1594-T112-06 and 15946T217-01. Each site of sampling was superposed with a local

deformation map in order to correlate strain localization with local passive layer thickness. Figure 15 is an example of such correlation for the sites 1A and 1B. The level of prior deformation E_{xx} in ambient air and second deformation E_{yy} in primary water corresponding to the sampling for TEM examinations are reported in Table 5.

Figure 16 shows the details of the oxide formed in site 1A. In this figure, the metal-oxide interface is clearly below the grid-oxide interface, suggesting the anionic growth of the inner Cr-rich oxide layer in the metal. The thickness of the oxide below the grid does not seem affected by the presence of the grid. A preferential oxidation can be also noticed within pre-established shear bands from prior deformation in air. Spinels (magnetite) grew on the inner Cr-rich oxide layer and on the grid. Spinels are in epitaxy with the metal, despite the presence of the inner Cr-rich oxide layer.

Figure 17 is a STEM observation of site 1B, showing the possible differences of density between

the outer and the inner part of the Cr-rich oxide layer. The outer part, at the interface with the spinels appears very regular and dense. This could be the result of the fine polishing including electro- then ionic polishing. By contrast, the inner part seems composed of small 'grains' growing inhomogeneously in the metal. The typical size of 'grains' observed in the inner oxide is similar to the fine dislocation structures in the underlaying metal.
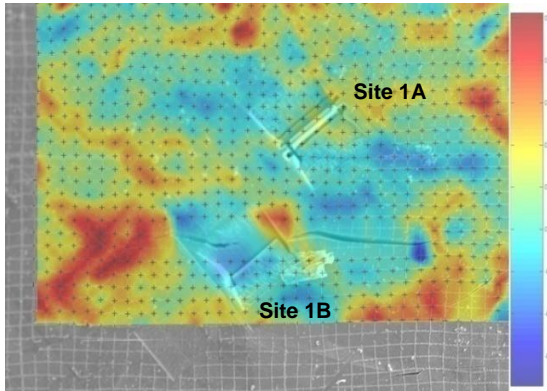

Figure 15 – Strain localization (second strain E_{yy}) in site 1 at the surface of specimen 1594-T112-06.
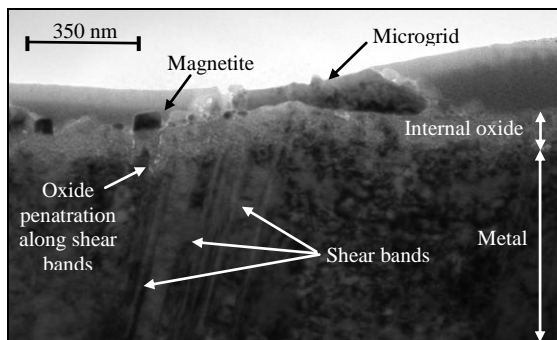

Figure 16 – Oxide observation (STEM, bright field) at the surface of specimen 1594-T112-06 (304L).
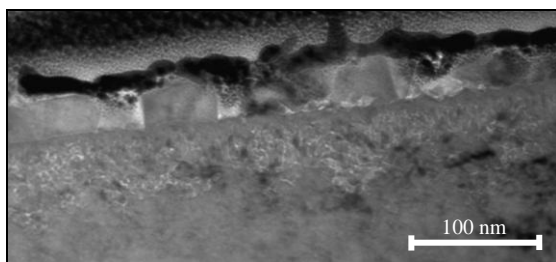

Figure 17 – STEM on site 1B at the surface of specimen 1594-T112-06 (304L).

Figure 18 indicates the position of the EDS scan presented in Figure 19. Shear bands are crossing the metal-oxide interface, and 'lines' are continuing in the oxide, suggesting that shear bands were emerging before testing in primary water. So, the more pronounced oxide penetration along slip bands probably result in prior deformation. The origin of the x-axis in Figure 19 is in metal. No O is observed during the EDX scan up to 120 nm. Nevertheless, in this range of position, a decrease of Fe content is associated to an increase of Ni content and a stable Cr content. In addition, the increase of

the Cr content is only observed for a position > 120 nm. The maximum concentration of Ni correspond to the position = 120 nm. This clearly indicates that oxidation at the metal-oxide interface (position > 120 nm) essentially results in Fe depletion followed by its diffusion within the inner oxide layer to the outer interface of Cr-rich oxide. Trends of O and Cr concentrations are similar in the metal and in the oxide. By contrast, trends of Ni and Fe concentrations are opposite in the metal and similar in the oxide. The Fe depleted zone in the metal is approximately 45 nm deep. The thickness of the Cr-oxide layer, affected by localized prior deformation, is about 100 nm. The mean chemical composition in the inner oxide is 50% Cr, 40% Fe and 10% Ni.
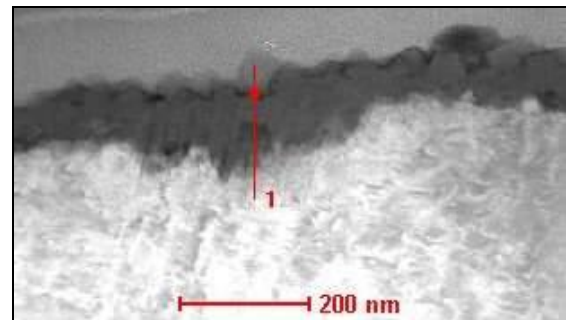

Figure 18 – Location of EDX profile on site 1A at the surface of specimen 1594-T112-06 (304L). STEM, HAADF detector.

Figure 20 indicates the position of the EDX scan presented in Figure 21. This last scan was realized perpendicularly to oxidized slip bands. On the most oxidized slip band, 50 nm ahead of the mean local metal-oxide interface, Fe content is 20% lower than Fe in the metal, 10 nm away. By contrast relative Cr content increases up to 17% and relative Ni content increases up to 56%. The Cr enrichment is observed approximately 6 nm away from the oxidized slip band. The Ni enrichment affects 10 nm, similarly to Fe depletion. The narrow oxidation of emerging slip bands is supposed to be a precursor of crack extension, limited to tens of nm, leading to initiation.
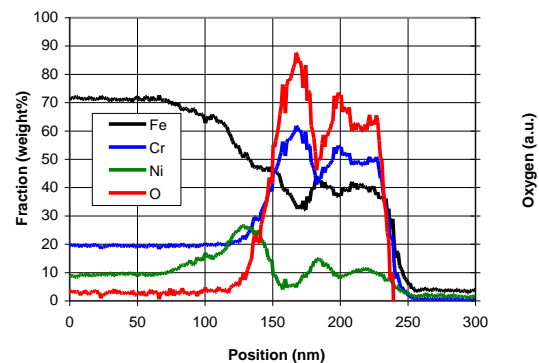

Figure 19 – EDX profile located in Figure 19. Site 1A at the surface of specimen 1594-T112-06 (304L).

Last, Figure 22 illustrates the significant porosity in the inner oxide layer, especially close to the metal-oxide interface. This important porosity could result in the local deformation ($E_{yy} = 0.075$) during
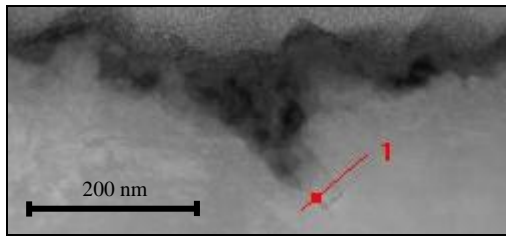
exposure to primary water.

Figure 20 – Location of EDX profile on site 2 at the surface of specimen 1594-T112-06 (304L). STEM, HAADF detector.
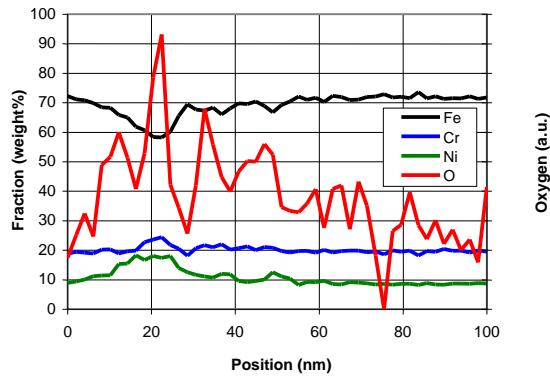

Figure 21 – EDX profile located in Figure 19. Site 2 at the surface of specimen 1594-T112-06 (304L).
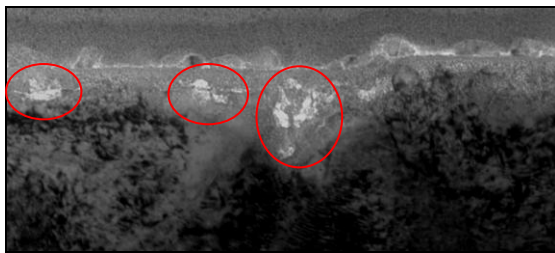

Figure 22 – Porosity in inner oxide layer, at the interface with the metal. STEM on site 2 at the surface of specimen 1594-T112-06 (304L).

Detailed analyses were done in order to evaluate the effect of strain localization on oxide penetration and on metal-oxide interface. Figure 23 is an example of EFTEM Cr-map. Figure 24 is the associated binary map obtained after filtering. Image analysis of this binary map allows to quantify the thickness of the inner Cr-rich oxide layer (Figure 25). In this situation, the mean oxide penetration is 50 nm. Finally, results obtained after image analysis of inner oxide layers are summarized in Table 5.
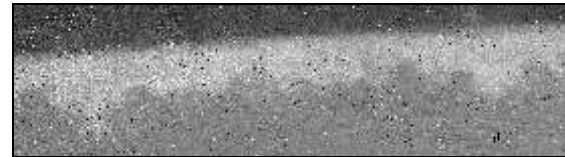

Figure 23 – Cr-mapping of oxide layer at the surface of specimen 1594-T112-06 (304L), in site 1B.

Figure 24. Binary Cr mapping of image presented in Figure 23. Specimen 1594-T112-06 (304L), in site 1B.
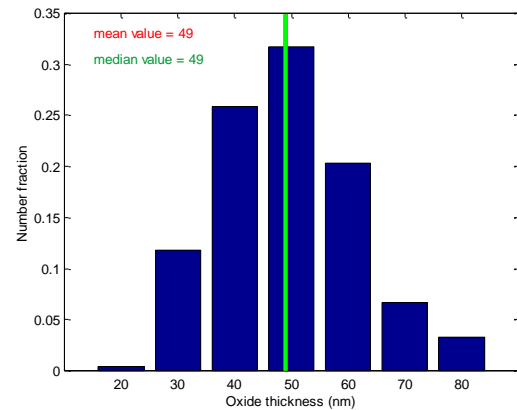

Figure 25. Distribution of the thickness of the rich-Cr inner oxide layer formed at the surface of specimen 1594-T112-06 (304L) after image analysis (Figure 24).

Table 5 – Analysis of Cr-rich inner oxide penetrations at the surface of the specimens.

Material	Site	Resolution (nm/pixel)	Local strain in the sample		Analysed length (nm)	Cr-rich inner oxide penetration (nm)				
			Prior E_{xx}	Second E_{yy}		Mean	Median	Min.	Max.	SD
304L	1A	2.82	0.10	0.02	1386	102	96	31	172	30
	1A	1.35	0.00	0.00	688	102	100	55	170	30
	1B	2.56	0.00	0.075	694	49	49	23	87	12
	2	1.41	0.02	0.07	679	81	82	54	101	9
316L	1G	5.88	0.02	0.10	1188	72	71	12	124	27
	1D	5.88	0.00	0.02	988	90	88	59	135	17
	2G	5.95	0.00	0.02	2077	46	48	6	101	25
	2D	1.72	0.10	0.01	890	73	74	40	105	14
	3G	5.88	0.10	0.01	2941	96	94	41	141	16
	3D	1.74	0.10	0.02	880	61	61	19	92	16

5.3. Crack tip examination

Thin foils were removed (dual beam sampling) at the surface of specimens 1594-T112-06 (304L) and 1594-T217-01 (316L). Active intergranular crack tips were observed. Indeed, contrary to usually observed crack propagation tips, there is a high probability that all of the tips observed are active, because they correspond to the earlier stage of initiation, before any branching and screening by other cracks. Cracks usually initiated where gradient of deformations are observed. Figure 26 and Figure 27 clearly exhibits cracks on grain boundaries separating grains with clear different densities of dislocations. Crack depth did not exceed few microns. Cracks are usually opened (Figure 26), 200 nm typically, in good agreement

with SEM observations at the surface (Figure 10). Opened cracks are filled with Fe oxide (Figure 28). A significant depletion of Fe is also observed up to 200 nm on the grain boundary, ahead of the tip. Similarly, a slight Cr depletion is observed on the grain boundary. Conversely, an important enrichment in Ni is observed.
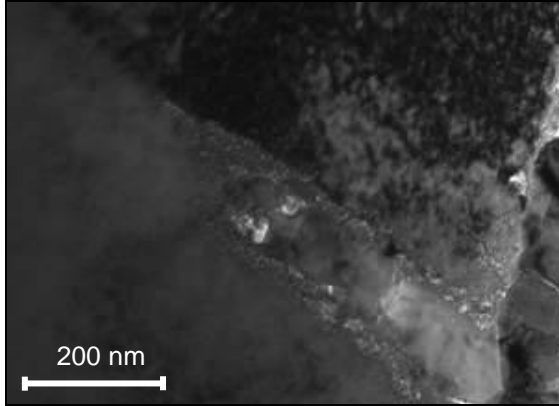

Figure 26. IGSCC initiated between grains with apparent different levels of deformation. Sampling on specimen 1594-T217-01 (316L), in site 2 (Prior-E_{xx} = 0, second E_{yy} = 0.03).
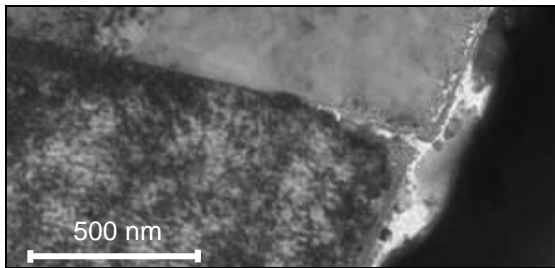

Figure 27. IGSCC initiated between grains with apparent different levels of deformation. Sampling on specimen 1594-T217-01 (316L), in site 3 (Prior-E_{xx} ≈ 0.1, second E_{yy} ≈ 0.03).
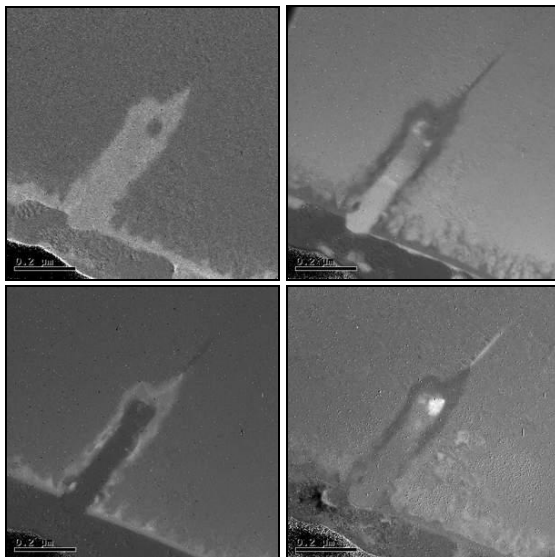

Figure 28. EFTEM O, Fe, Cr and Ni maps on an intergranular crack initiated between grains with apparent different levels of deformation. Sampling on specimen 1594-T217-01 (316L), in site 2 (Prior-E_{xx} = 0, second E_{yy} = 0.03).

6. RESULTS OF FEM

6.1. Identification of crystal plasticity law

The identification of the crystal plasticity law of the 304L is based on:

- Monotonic tensile tests at 20°C ($\dot{\varepsilon}$ = 2 10^{-3} s^{-1}) and at 360°C ($\dot{\varepsilon}$ = 10^{-6} s^{-1}).
- Monotonic shear tests at 20°C ($\dot{\gamma}$ = 10^{-3} s^{-1}, $\dot{\gamma}$ = 10^{-1} s^{-1}).
- Cyclic shear test at 20°C (2 cycles, $\Delta\gamma/2$ = 0.1, $\dot{\gamma}$ = 10^{-3} s^{-1}).
- Cyclic hardening at 20°C (50 cycles, $\Delta\varepsilon$ = ± 0.024, $\dot{\varepsilon}$ = 4 10^{-3} s^{-1}).
- Creep test at 20°C under constant load (250 MPa, 216 h) and under trapezoidal load (σ_{min} = 250 MPa, σ_{min} / σ_{max} = 0.8, hold time = 3420 s, unload time = 90 s, reload time = 90 s, 201 h).
- Creep test at 360°C (250 MPa, 6000h), including the preloading tension curve ($\dot{\varepsilon}$ = 10^{-3} s^{-1}). Creep rate is very low ($\dot{\varepsilon}$ = 1.7 10^{-12} s^{-1}).
- Creep test at 360°C (400 MPa, 8000h), including the preloading tension curve ($\dot{\varepsilon}$ = 10^{-3} s^{-1}). Creep rate is very low ($\dot{\varepsilon}$ = 2.8 10^{-12} s^{-1}).
- Non-isothermal (20°C-360°C) relaxation at 250MPa and 350MPa
- Cross test (complex loading path) including:
  - Prior-tension ε_1 = 0.31, 20°C, 2 10^{-3} s^{-1}
  - Loading (ε_2 = 0.06, 360°C, 2 10^{-3} s^{-1}) of a secondary specimen removed at 90° from the pre-tension axis.

The elasto-viscoplastic constitutive law was identified by homogenization approach. The procedure of identification was the following:

- Isotropic elasticity was supposed, Young's modulus (E =185000 MPa) and Poisson's ratio (ν = 0.3) were taken from ASTM Material Handbook.
- Yield limit (τ_0) was evaluated has the ratio of the macroscopic yield strength (170 MPa) and the mean value of the resolved shear stress (2.65).
- If no explicit information is available for the interaction matrix the first estimation is h_{rs} = 1.
- For the creep power law, the value n = 7 was initially taken, in agreement with deformation-mechanism maps proposed by Frost and Ashby (8) for the same material.
- High value of kinematic hardening (d) was chosen, in order to fit the first cyclic loading on kinematic hardening, while low value of isotropic hardening (b) was

chosen to fit the following cycles of loading on isotropic hardening.

Experimental data at room temperature (20°C) were used for the first identification. The final set of parameters is presented in Table 6.

Table 6 – Material parameters after identification.

Temp. (°C)	E (MPa)	ν	τ_0 (MPa)	Q	b	K_s (MPa.s$^{1/n}$)	n	c	d
20	200000	0.3	65	45	3	65	7	600	20
360	185000	0.3	50	45	3	10	4	600	20

6.2. Effect of the strain path on stress and strain distributions

Parallel computations were done, after subdomain decomposition, in order to distribute the computations on different processors of the cluster. A complex loading path was applied, including prior-elongation in 20 s till 2% in direction $\vec{x}$, unloading in 5 s and a second elongation in 20 s till 2% in perpendicular direction $\vec{y}$.

Figure 29 shows the significant gradient of Von Mises stress after a 2% pre-deformation (a), especially at grain boundaries, and the important increase of such a gradient after a change of strain path (b). Computations on the aggregates allow exhibiting the heterogeneity of the equivalent stress (Von Mises) and of the strain fields. Figure 30 shows distribution of ε_{xx} at the end of pre-loading in direction $\vec{x}$ (mean(ε_{xx}) = 0.02) and for an intermediate deformation (mean(ε_{xx}) = 0.01). More precisely, we can see the increase of the heterogeneity of ε_{xx} when mean deformation increases. For example, ε_{xx} is in the range 0.002–0.020 after 1% elongation, while ε_{xx} is in the range 0.005–0.040 after 2% elongation. By contrast, there is no significant evolution of stress σ_{xx} in the same range of deformation.

To appreciate the implications of the slip systems selected, the Taylor factor M has been calculated. M can be defined (12) as the sum of the slip on all crystallographic slip systems s, divided by the norm of inelastic strain tensor ε_p.

$$M = \frac{\sum_s |\gamma^s|}{|\varepsilon_p|} \quad (12)$$

Therefore, high M values are expected when the orientation is not favorable for gliding, or when several slip systems are required to accommodate the strain incompatibilities. Figure 31 indicates a severe impact from the change of strain path on the distribution of the Taylor factors: first, an important positive shift of M is observed, corresponding to the activation of a significant number of additional slip systems to accommodate the deformation; second, the distribution of M is more symmetric after a change of strain path. The asymmetry in the distribution of M indicates that most of the

deformation implies one slip system (lower M values), while a limited part of the deformation involves multiple slips (higher M values).
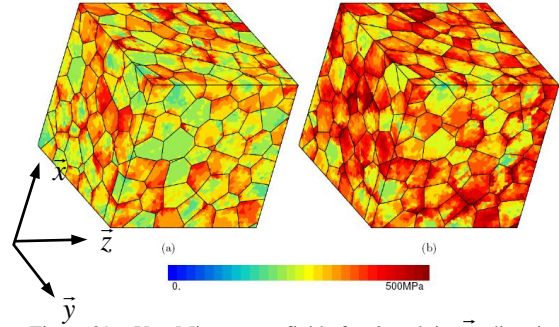

Figure 29 – Von Mises stress field after 2% el. in $\vec{x}$ direction (a) and after additional 2% el. in $\vec{y}$ direction (b). Computations on 304L.
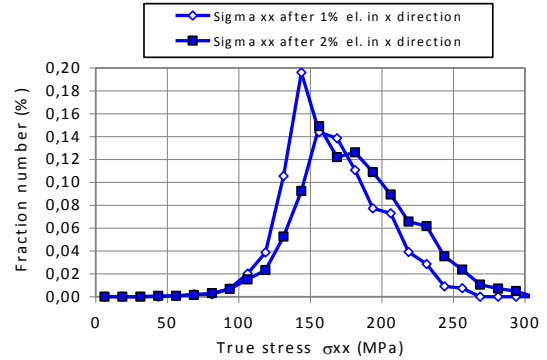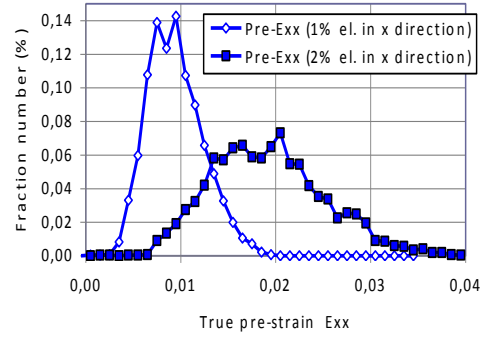

Figure 30 – Distribution of ε_{xx} and σ_{xx} at an intermediate prior deformation (mean(ε_{xx}) = 0.01) and at the end of pre-loading (mean(ε_{xx}) = 0.02) in direction $\vec{x}$. Computations on 304L.
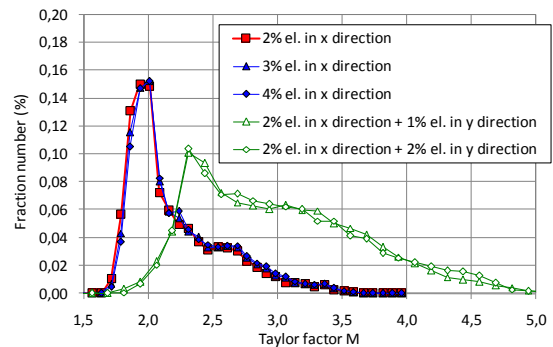

Figure 31 – Evolution of M due to the change of strain path. Computations on 304L.

7. DISCUSSION

7.1. Correlation between strain hardening and oxidation

Results obtained after image analysis of inner oxide layers are plotted in Figure 32. These results suggest an increase of the mean oxide penetration with the local cumulated equivalent deformation E_{axial}^{cum}. The evolution of the maximum oxide penetration $\max(p)$ against E_{axial}^{cum} follows an ATAN law, given in (13):

$$\max(p) = 140 + 26ATAN\left(125E_{axial}^{cum} - 12\right) \qquad (13)$$

where p is in nm. By contrast, the mean penetration increased linearly with E_{axial}^{cum}. Typically, the maximum and the mean oxide penetrations increased by a factor 2 when 12% of axial deformation is reached. The increase of the mean value of the Cr-rich layer could indicate the decrease of the efficiency of passivity property of the oxide when strain hardening increases. This could result in the effect of the local non-homogeneous diffusion in the metal on the microstructure of the oxide (grain size) and associated transport properties. Previous studies (9) already mentioned the increase of the Cr-rich oxide layer with pH in primary water, associated to an increase of the IGSCC susceptibility. Thus, both mechanical and chemical properties are susceptible to alter the properties of the passive layer formed at the surface of stainless steels exposed to primary environment. The alteration of these properties promotes SCC initiation when, in addition, local stress concentration can fracture the passive layer.
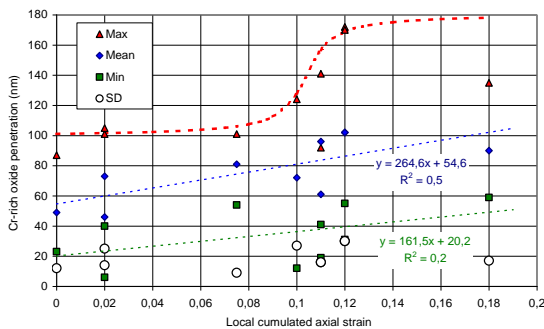

Figure 32 – Evolution of Cr-rich oxide penetration (min., mean, max., SD) at the surface of 304L stainless steel as a function of local cumulated axial strain E_{axial}^{cum}.

7.2. Correlation between loading and initiation

Most cracks identified in this study are intergranular. Nevertheless, shallow transgranular cracking also initiated. By contrast, following a simple monotonic strain path, pure trans-granular stress corrosion cracking is usually observed (2). Therefore, complex loading promotes intergranular initiation of SCC.

Strain is not homogeneous by nature. In this study, distribution of deformation levels were measured and calculated at the scale of the polycrystal. Local stress and especially intergranular stress are associated with strain heterogeneity. Strain heterogeneity at the scale of the polycrystal aggregate seems to control possible sites of cracking. Indeed, cracks initiate where the strain gradients are important. Therefore, intergranular stress due to strain incompatibilities seems to drive the stress corrosion cracking mechanism. Consequently, slip traces intersecting intergranular cracks are often observed on one grain adjacent to the crack. The typical range of angle of intersection is 45° to 90°. This observation also is in good agreement with previous observations of intergranular crack tip (9).

7.3. Assumed mechanism

Based on previous considerations, the following basic mechanism is assumed to describeboth initiation and propagation of SCC in stainless steels exposed to primary water:

1. Oxidation, leading to the formation of a superficial Cr-rich passive layer with a mean thickness of 50 nm. The maximum oxide penetration does not exceed 100 nm at 360°C, when $7 < pH_{320°C} < 8$, if the material is not strain hardened. Nevertheless, the mean and maximum oxide penetrations increase for higher pH values and when the material is strain hardened.

2. When sufficient, local stresses lead to the fracture of the oxide or metal-oxide interface. Strain hardening, loading fluctuations, intergranular strain incompatibilies and irregular metal-oxide interfaces promote stress concentrations and, as a consequence, initiation or crack tip extension. Changes of strain path enhance stress concentrations on the grain boundaries.

8. CONCLUSION

Understanding and quantification of interactions between localized deformation in materials and environmental-assisted cracking could play role in maintaining the integrity of LWR components. Thus, a detailed understanding of strain localization during plastic deformation and of the underlying mechanisms is important for the manufacture and design of materials exposed to the environment of the primary circuit of PWRs.

The objectives of this study was to evaluate the relevance of interactions between localized deformation and initiation of stress corrosion cracking in austenitic stainless steels exposed to a

PWR primary environment and to correlate quantitatively strain localization and selective oxidation. Experimental investigations and computations helped to quantify the effect of a change of strain path on strain localization and to increase understanding of the contribution of local strain and stress on SCC.

Works are in progress in order to evaluate strain localization effect on oxidation and IGSCC of Ni-based alloys.

Future works will focus on the coupling of identified mechanisms (deformation, oxidation, fracture) in order to model initiation.

REFERENCES

1. **HICKLING**, 'Understanding the interaction between localized deformation in materials and environmently assisted cracking', EPRI technical report 1011789, 2005.

2. **T. COUVANT, F. VAILLANT, JM. BOURSIER, D. DELAFOSSE**, 'Effect of strain path on SCC of AISI 304L stainless steel in PWR primary environment at 360°C' (Paper presented at Eurocorr'2004, Nice, France, 2004).

3. **SCHMITT, AERNOUDT, BAUDELET**, 'Yield loci for polycristalline metals without texture', Material Science and Engeneering, 75 (1985), 13-20.

4. **ANGEL**, 'Formation of martensite in austenitic stainless steels', *Journal of the Iron and Steel Institute*, 177 no 1 (1954), 165-174.

5. **LACOMBE**, **BERANGER**, 'Structures et diagrammes d'équilibre des diverses nuances d'acier inoxydables. Conséquences sur leurs traitements thermiques', Les aciers inoxydables, éd. P. Lacombe, pp. 13-58, 1990.

6. **G. CAILLETAUD**, 'A micromechanical approach to inelastic behaviour of metals', International Journal of Plasticity, Volume 8, Issue 1, 1992, Pages 55-73.

7. **J. BESSON, R. LE RICHE, R. FOERCH, G. CAILLETAUD**, 'Object-oriented programming applied to the finite element method. Part II: application to material behaviors', Rev. Eur. Elements Finis 7, 567–588. 1998.

8. **H. J. FROST, M. F. ASHBY**, 'Deformation-Mechanism Maps, The Plasticity and Creep of Metals and Ceramics', Cambridge University, UK. http://engineering.dartmouth.edu/defmech/.

9. **T. COUVANT, L. LEGRAS, C. POKOR, F. VAILLANT, Y. BRECHET, J.M. BOURSIER, P. MOULART,** 'Investigations on the mechanisms of PWSCC of strain hardened austenitic stainless steels', 13th International Conference on environmental degradation of materials in nuclear systems-water reactors, Whistler (Canada), 2007.